JACS
JOURNAL OF THE AMERICAN CHEMICAL SOCIETY
Article
pubs.acs.org/JACS

Nanocatalyst Superior to Pt for Oxygen Reduction Reactions: The Case of Core/Shell Ag(Au)/CuPd Nanoparticles

Shaojun Guo,[†,∥] Xu Zhang,[‡] Wenlei Zhu,[†] Kai He,[§] Dong Su,[§] Adriana Mendoza-Garcia,[†] Sally Fae Ho,[†] Gang Lu,*[,‡] and Shouheng Sun*[,†]

[†]Department of Chemistry, Brown University, Providence, Rhode Island 02912, United States
[‡]Department of Physics and Astronomy, California State University, Northridge, California 91330, United States
[§]Center for Functional Nanomaterials, Brookhaven National Laboratory, Upton, New York 11973, United States

Supporting Information

ABSTRACT: Controlling the electronic structure and surface strain of a nanoparticle catalyst has become an important strategy to tune and to optimize its catalytic efficiency for a chemical reaction. Using density functional theory (DFT) calculations, we predicted that core/shell M/CuPd (M = Ag, Au) NPs with a 0.8 or 1.2 nm $CuPd_2$ shell have similar but optimal surface strain and composition and may surpass Pt in catalyzing oxygen reduction reactions. We synthesized monodisperse M/CuPd NPs by the coreduction of palladium acetylacetonate and copper acetylacetonate in the presence of Ag (or Au) nanoparticles with controlled shell thicknesses of 0.4, 0.75, and 1.1 nm and CuPd compositions and evaluated their catalysis for the oxygen reduction reaction in 0.1 M KOH solution. As predicted, our $Ag/Cu_{37}Pd_{63}$ and $Au/Cu_{40}Pd_{60}$ catalysts with 0.75 and 1.1 nm shells were more efficient catalysts than the commercial Pt catalyst (Fuel Cells Store), with their mass activity reaching 0.20 A/mg of noble metal at −0.1 V vs Ag/AgCl (4 M KCl); this was over 3 times higher than that (0.06 A/mg Pt) from the commercial Pt. These Ag(Au)/CuPd nanoparticles are promising non-Pt catalysts for oxygen reduction reactions.

INTRODUCTION

Recent advances in energy research call for the rational design and synthesis of catalysts with unprecedented efficiency in catalyzing energy conversion reactions,[1−4] especially the oxygen reduction reaction (ORR).[5−8] Numerous studies on ORR have focused on catalysts with ultralow Pt contents, with both electronic and geometric effects being used to explain ORR catalysis. Electronic effects result in charge redistribution on the surface of the catalysts, making the catalytic sites "hotter",[9−13] while geometric effects often put shape and atom distance in consideration to tune the binding strength between Pt and O.[14−16] Pt−O bonding on a perfect Pt(111) is calculated to be 0.2 eV stronger than the optimal level (ΔE = −0.2 eV),[17,18] and a compressed Pt strain on the catalyst surface may help to weaken the Pt−O bond and to enhance ORR catalysis.[13−16] Experimentally, a variety of Pt-based alloy and core/shell nanoparticles (NPs) have been designed, synthesized, and tested to improve oxygen dissociative adsorption on Pt and Pt−O desorption for Pt surface regeneration.[19−32] A more important aspect is to develop a non-Pt catalyst with catalytic power comparable to or even superior to that of Pt.[33,34] Studies on energetics of oxygen dissociative adsorption on 1 nm Pd shells with a series of core metals have shown that tuning charge redistribution and surface strain can change the d-band center of the Pd shell and, thus, oxygen dissociative adsorption energy. For this reason, core/shell Cu/Pd, Co/Pd, and Mo/Pd systems may be similar to Pt in catalyzing ORRs.[35] In contrast, the presence of a more electronegative Au core does not favor the increase in Pt activity for the ORR, but the Au core can help to enhance shell stability.[28]

Considering Au (or Ag) core and Cu alloy effects on Pd ORR catalysis,[35] we chose to study a ternary system based on core/shell Ag/CuPd or Au/CuPd NPs to understand how the Ag (or Au) core and CuPd alloy effects can be used to tune and optimize Pd catalysis for the ORR. Herein, we present our study on tuning M/CuPd (M = Ag, Au) into the active ORR catalyst in 0.1 M KOH solution. The unique aspect of the ternary core/shell M/CuPd for ORR is that it allows the dual tuning of both surface strain and composition to achieve more rational control on catalytic properties and to facilitate catalysis optimization. Our computational and experimental data both show that CuPd alloy composition and shell thickness are important to control the ORR activity of the Ag/CuPd NPs. The optimal Cu concentration and CuPd shell thickness are 37(±3)% and ∼1 nm, respectively. Au as a core in the core/shell structure can further improve CuPd catalysis for the ORR. Among the different catalysts studied, including Ag, CuPd, Ag/CuPd, and Au/CuPd as well as commercial Pt, Ag/CuPd and Au/CuPd core/shell NPs under the optimal tuning show the

Received: August 12, 2014
Published: October 3, 2014

   dx.doi.org/10.1021/ja508256g | J. Am. Chem. Soc. 2014, 136, 15026−15033

highest mass activity for the ORR at 0.18 and 0.20 A/mg of noble metal, respectively, at −0.1 V (vs Ag/AgCl) and retain 77.6% of this activity after 48000 s $i-t$ test. As a comparison, the commercial Pt catalyst (Fuel Cells Store) has a mass activity of 0.06 A/mg of Pt and retains 62.9% activity after the same stability test. Our studies demonstrate an important route to the rational design and synthesis of highly active non-Pt catalysts for the ORR.

EXPERIMENTAL METHODS AND COMPUTATIONAL MODELS

Chemicals and Materials. Oleylamine (OAm, >70%), 1-octadecene (ODE), oleic acid (OA), palladium acetylacetonate ($Pd(acac)_2$), copper acetylacetonate ($Cu(acac)_2$), $HAuCl_4{\cdot}H_2O$, silver nitrate, 1,2-tetradodecanediol, hexane, isopropyl alcohol, ethanol, and Nafion (5%) were all purchased from Sigma-Aldrich. The C−Pt (20% mass loading, mainly 2.5−3.5 nm in diameter) catalyst was obtained from Fuel Cell Store.

Instrumentation. Transmission electron microscopy (TEM) images were obtained with a Philips CM 20 instrument operating at 200 kV. Scanning transmission electron microscopy (STEM) analyses were carried out using a Hitachi HD2700C (200 kV) with a probe aberration corrector, at the Center for Functional Nanomaterials at Brookhaven National Laboratory. The 2D electron energy-loss spectroscopy (EELS) mapping was collected using a high-resolution Gatan-Enfina ER instrument with a probe size of 1.3 Å. A power law function was used for EELS background subtraction. X-ray diffraction (XRD) characterization was carried out on a Bruker AXS D8-Advanced diffractometer with Cu Kα radiation (λ =1.5418 Å). The inductively coupled plasma-atomic emission spectroscopy (ICP-AES) measurements were carried on a JY2000 Ultrace ICP Atomic Emission Spectrometer equipped with a JY AS 421 autosampler and 2400g/mm holographic grating. Samples for TEM analysis were prepared by depositing a single drop of diluted nanoparticle dispersion in hexane on amorphous carbon coated copper grids. The electrochemical measurements on a glassy-carbon (GC) electrode using Ag/AgCl (vs 4 M KCl) as the reference electrode and platinum wire as the counter electrode, respectively, were performed on a potentiostat (Autolab 302N).

Synthesis of 3.1 nm Ag and Au NP. A 0.38 g portion of $AgNO_3$ was mixed with 20 mL of OAm and 0.4 mL of OA, and the magnetically stirred mixture was heated to 120 °C for 18 h. The solution was then cooled to room temperature. A 30 mL portion of acetone was added to precipitate the product. The product was separated by centrifugation at 9000 rpm for 10 min, washed with ethanol, and redispersed in hexane.

Au NPs with different sizes were synthesized according to the reported protocols.[36]

Synthesis of Ag/CuPd NPs. In a typical synthesis of $Ag/Cu_{37}Pd_{63}$ NPs, 30 mg of $Pd(acac)_2$ and 26 mg of $Cu(acac)_2$ were mixed with 10 mL of ODE, 1.0 mL of OAm, 1.0 mL of OA, and 0.2 g of 1,2-tetradodecanediol. The magnetically stirred solution was then heated to 80 °C under N_2 protection. A 30 mg portion of Ag seeds dispersed in 2 mL of ODE was rapidly injected into the above solution, which was further heated to 200 °C at a heating rate of 4−5 °C/min. The solution was heated to 200 °C for 25 min and cooled to room temperature. Isopropyl alcohol was added to precipitate the product. The product was separated by centrifugation at 9000 rpm for 10 min, washed once with isopropyl alcohol and then ethanol, and redispersed in hexane.

Similarly, replacing Ag NPs with 40 mg of Au NPs gave Au/CuPd NPs.

Synthesis of 3.5 nm $Cu_{40}Pd_{60}$ NPs. $Cu_{40}Pd_{60}$ NPs (3.5 nm) were synthesized according to the reported protocols.[37] In a typical synthesis, 0.30 mmol of $Cu(acac)_2$ and 0.30 mmol of $Pd(acac)_2$ were dissolved in 3 mL of OAm. This solution was then injected into a mixture of morpholine−borane (1.5 mmol), 3 mL of OAm, and 7 mL of ODE at 80 °C. The resulting mixture was subsequently heated to 100 °C and kept at that temperature for 1 h. Finally, the NPs were washed in a mixture of acetone and isopropyl alcohol and centrifuged two times at 9000 rpm for 10 min before redispersing them in hexane.

NP Catalyst Preparation. A 20 mg portion of NPs dispersed in 20 mL of hexane and 40 mg of Ketjen carbon dispersed in 30 mL of hexane were mixed and further sonicated with a Fisher Scientific FS 110 instrument for 1 h to prepare C-NPs. The product was separated by centrifugation, washed twice with hexane, dried under ambient conditions, and further heated in the air at 150 °C overnight to remove the surfactant. The heat-treated C-NPs were redispersed in a mixture containing water, isopropyl alcohol, and Nafion (5%) (4/1/0.05 v/v/v) to form a 4 mg/mL suspension.

Electrochemistry. Prior to the surface coating, the GC electrode (5 mm in diameter) was polished with 1.0 and 0.05 μm alumina powders, respectively, and rinsed with deionized water, followed by successive sonications in ethanol and doubly distilled water. The electrode was allowed to dry under nitrogen. A 5 μL portion of catalyst ink was cast on the GC electrode and dried. The counter electrode was Pt wire, and the reference electrode was Ag/AgCl (4 M KCl). The electrolyte was N_2-saturated 0.1 M KOH solution. All of the catalyst electrodes were cleaned with a steady-state CV in the range of −0.8 to +0.1 V (vs Ag/AgCl) at 100 mV/s for 20 cycles. ORR measurements were conducted in O_2-saturated 0.1 M KOH solution. The disk rotation rate was set at 1600 or 400 rpm. The potential scan rate was at 10 mV/s.

Calculations of ΔE_O on Intermetallic CuPd Surface. The E_O value was determined by placing an O atom on the *fcc* hollow site following

$$E_O = E[\mathrm{PdCu{+}O}] - E[\mathrm{PdCu}] - E[\mathrm{O_2}]/2$$

where E[PdCu+O] and E[PdCu] are total energies of the PdCu alloy surface with and without O adsorbate, respectively. $E[O_2]$ is the total energy of a oxygen molecule. For DFT calculations of total energies, we used 3×3 $(\sqrt{3} \times \sqrt{3})R30°$ surface unit cells. A four-layer slab was used for these calculations with the top two layers fully relaxed. The optimal E_O value is 0.2 eV higher than that on a Pt(111) flat surface.[17,18] The ΔE_O value was then calculated by shifting E_O relative to this optimal value.

Calculation of Surface Strain on Core/Shell NPs. We construct the cuboctahedral models to represent core/shell NPs as shown in Figure 1b,d. To model the random alloy shell, 10 randomly generated atomic structures were examined to provide the strain distribution. All atoms were fully relaxed by the embedded atom method (EAM) interatomic potentials.[38] There are eight (111) facets in the cuboctahedral NP, and for each (111) facet we selected three O-adsorbed sites (*fcc* hollow sites) to measure the local strain. Thus, for each NP model, 240 sites were included in the strain distribution.

Calculation of Interfacial Energy. Two 4×2 slabs with four atomic layers were used to calculate the interfacial energy (Figure 1f), with the bottom two layers being the core material M (M = Au, Ag). The left part of Figure 1f corresponds to the Pd|Cu|M interface and the right part to the Cu|Pd|M interface. The interfacial energy difference is defined as

$$\Delta E[\mathrm{M}] = E[\mathrm{Pd|Cu|M}] - E[\mathrm{Cu|Pd|M}]$$

where E[Pd|Cu|M] and E[Cu|Pd|M] are the total energies of the Pd|Cu|M and Cu|Pd|M interfaces, respectively.

Computational Parameters. The DFT calculations were carried out using the VASP package[39,40] with the projector augmented wave pseudopotentials (PAW)[41] and Perdew−Burke−Ernzerhof generalized gradient approximation (PBE-GGA).[42] An energy cutoff of 400 eV was used for the plane-wave basis set. The Brillouin zone was sampled on the basis of the Monkhorst−Pack scheme with a $3 \times 3 \times 1$ k-point mesh.[43]

RESULTS AND DISCUSSION

Computational Studies of M/CuPd NPs. To understand the effects of alloy composition, shell thickness, and core material of M/CuPd NPs on Pd−O bonding and further on the

dx.doi.org/10.1021/ja508256g | J. Am. Chem. Soc. 2014, 136, 15026−15033

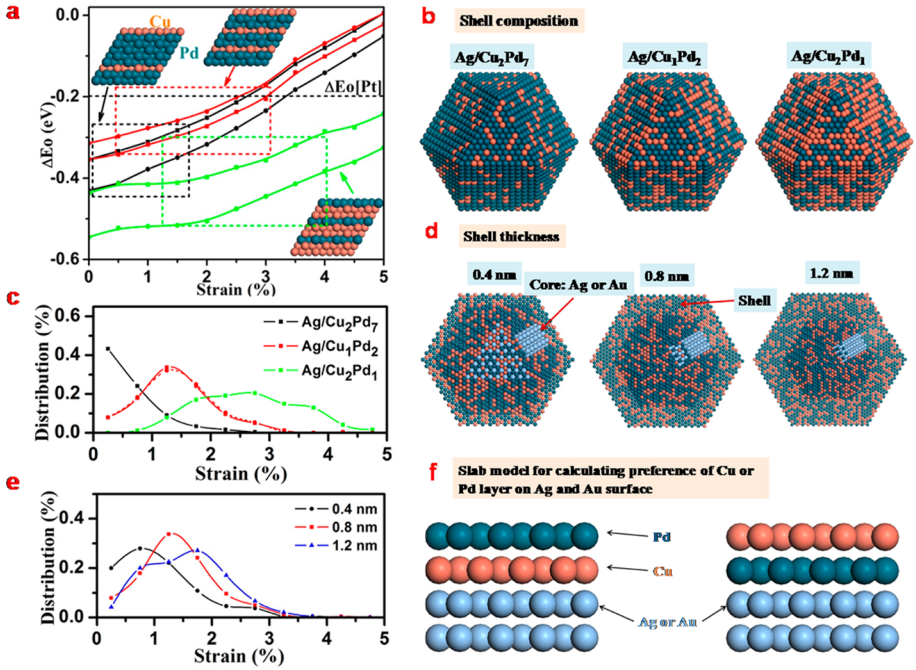

Figure 1. (a) ΔE_O as a function of strain and composition. Black, red, and green curves represent Cu/Pd atomic ratios of 2/7, 1/2, and 2/1, respectively. Several curves in each color correspond to various *fcc* hollow sites for O adsorption. ΔE_O on the Pt(111) surface is indicated by the dashed horizontal line. Black, red, and green boxes outline the possible ΔE_O values on Ag/Cu_2Pd_7, $Ag/CuPd_2$, and Ag/Cu_2Pd NPs, respectively. (b, c) Models of core/shell NPs for various shell compositions with a shell thickness of 0.8 nm (b) and evaluated distribution of surface strain on these core/shell NPs (c). The dashed curve in (c) indicates $Au/CuPd_2$ NPs. (d, e) Models of core/shell NPs for various shell thickness with a composition of $CuPd_2$ (d) and evaluated distribution of surface strain on these core/shell NPs (e). (f) Slab models for calculation of Pd|Cu|M (left) and Cu|Pd|M (right) interfacial energies.

ORR activity, we employed density functional theory (DFT) to analyze the oxygen adsorption energy (E_O), a commonly used descriptor for ORR activity, on different kinds of NP surfaces.[17,18] Since oxygen overbinds to Pd and Cu surfaces (ΔE_O is negative), the goal is to design CuPd alloys with less negative ΔE_O values to achieve higher ORR activities. First, we focus on the dependence of ΔE_O on the surface strain and chemical composition of intermetallic CuPd (the disordered CuPd alloys have similar dependence; see Figure S1 (Supporting Information). Specifically, three chemical compositions with Cu/Pd atomic ratios of 2/7, 1/2, and 2/1, each under a compression from 0 to 5%, were examined. Figure 1a depicts ΔE_O as a function of the surface strain and chemical composition on the flat (111) surface of the CuPd alloys. We see a monotonic increase of ΔE_O with respect to the compression of the alloys. Since Cu has a smaller lattice constant than Pd, alloying more Cu would increase the compression and ΔE_O value. However, a large Cu concentration (green curves in Figure 1a) actually lowers ΔE_O, which is consistent with the fact that oxygen binds too strongly on the Cu surface. Hence, there is a competition between the strain and chemical effects with respect to Cu concentration.

Three cuboctahedral NP models are constructed to represent Ag/Cu_xPd_y with x/y = 2/7, 1/2, and 2/1, and these core/shell NPs have the same core diameter of 3.2 nm (16 atomic layers) and shell thickness of 0.8 nm (4 atomic layers) (Figure 1b). All CuPd alloy shells are set to have a solid solution structure to estimate the strain distribution on the shells. As shown in Figure 1c, the higher the Cu concentration in the alloy, the greater the compressive strain on the NP surface. On the basis of the strain distributions and the alloy compositions, we estimated the ΔE_O distribution for each NP as indicated by the dashed boxes in Figure 1a. The horizontal and vertical positions of each box represent the range of the strain and ΔE_O distribution for each NP, respectively. The ORR activity of the core/shell NPs is ranked as $Ag/CuPd_2$ > Ag/Cu_2Pd_7 > Ag/Cu_2Pd and the optimized Ag/CuPd NPs even surpass Pt for the ORR.

We chose $Ag/CuPd_2$ NPs to study the shell thickness effect on the ORR. Three different core/shell NPs with shell thicknesses of 0.4, 0.8, and 1.2 nm were examined, and their structures and surface strain distributions are shown in Figure 1d,e. We can see that the shell becomes more compressive as the thickness increases. The $Ag/CuPd_2$ NPs with 0.8 and 1.2 nm shell thicknesses show the strain distributions similar to but better than those with 0.4 nm shells for the ORR. Since the NPs have the same chemical composition and only the strain effect is at play, we conclude that for $Ag/CuPd_2$, either a 0.8 or a 1.2 nm CuPd shell would have a higher ORR activity.

To study the core effect on CuPd shell strain, we replaced Ag with Au and calculated the surface strain distribution (Figure 1c). We can see that surface strain distributions are independent of the core materials. We calculated the interfacial energy between the PdCu shell and the core (Au or Ag). For simplicity, we modeled the shell by a bilayer Pd|Cu (Pd on top of Cu) vs Cu|Pd (Cu on top of Pd) (Figure 1f). When the core is Au, the Pd|Cu|Au interface is energetically more stable than the Cu|Pd|Au interface with an energy difference of −264 mJ/m^2. If the core is Ag, the Pd|Cu|Ag interface is energetically less stable than the Cu|Pd|Ag interface with an energy difference of +5 mJ/m^2. Therefore, with Au as the core, it is energetically favorable for Pd to segregate at the NP surface, leading to higher ORR activity.

dx.doi.org/10.1021/ja508256g | J. Am. Chem. Soc. 2014, 136, 15026−15033

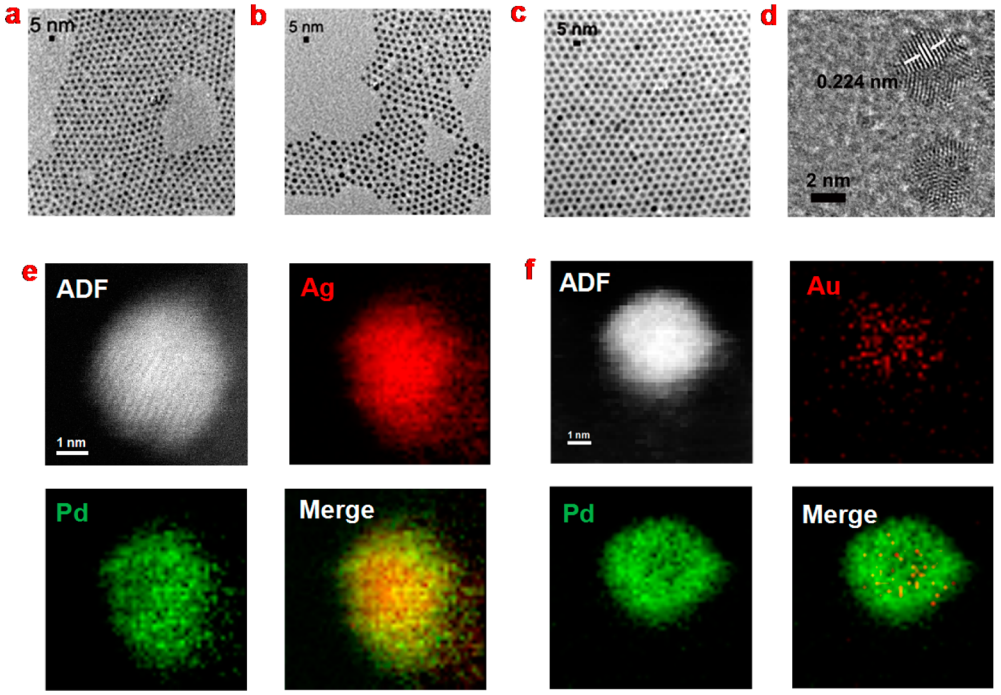

Figure 2. (a–c) TEM and (d) HRTEM images of (a) Ag, (b, d) Ag/$Cu_{37}Pd_{63}$, and (c) Au/$Cu_{40}Pd_{60}$. (e, f) STEM-EELS mapping (29 × 66 pixels, spatial resolution of 3 Å) images of (e) 4.6 nm Ag/$Cu_{37}Pd_{63}$ and (f) 4.6 nm Au/$Cu_{40}Pd_{60}$ NPs.

Synthesis of M/CuPd NPs. Our computational results indicate that Ag/$CuPd_2$ NPs with 0.8 and 1.2 nm shell thicknesses may surpass Pt on catalysis for the ORR and replacing Ag with Au can further optimize the ORR catalysis. To confirm these predictions, we developed a seed-mediated growth method to prepare monodipserse core/shell M/CuPd NPs for electrocatalytic studies of ORR. In the synthesis of Ag-based core/shell NPs, we first prepared monodisperse Ag NPs by reacting 380 mg of silver nitrate with 20 mL of OAm in the presence of 0.4 mL of OA at 120 °C for 18 h (see Experimental Methods and Computational Models). Figure 2a shows the typical TEM image of the Ag NPs. The Ag NPs have an average size of 3.1 ± 0.2 nm. To synthesize Ag/CuPd NPs, 30 mg of $Pd(acac)_2$ and 26 mg of $Cu(acac)_2$ were added to a solution of 10 mL of ODE, 1.0 mL of OAm, 1.0 mL of OA, and 0.2 g of 1,2-tetradodecanediol, and the solution was heated to 80 °C. A 30 mg portion of Ag seeds dispersed in 2 mL of ODE was added to the above mixture, and the solution was further heated to 200 °C for 25 min. The product was precipitated out by adding isopropyl alcohol and washed with isopropyl alcohol and ethanol, respectively, before it was dispersed in hexane. Inductively coupled plasma-atomic emission spectroscopy (ICP-AES) was used to measure the composition of the as-prepared Ag/CuPd NPs. The synthesis yielded Ag/$Cu_{37}Pd_{63}$ with a 0.75 ± 0.05 nm shell, denoted as Ag/$Cu_{37}Pd_{63}$-0.75 (Figure 2b). With the amount of Ag NPs and $Pd(acac)_2$ fixed, the composition of the CuPd shell could be tuned by controlling the molar ratio of $Pd(acac)_2$ to $Cu(acac)_2$. Under the same reaction conditions as in the synthesis of Ag/$Cu_{37}Pd_{63}$ NPs, 30 mg of $Pd(acac)_2$ + 13 mg of $Cu(acac)_2$, and 30 mg of $Pd(acac)_2$ + 52 mg of $Cu(acac)_2$ resulted in Ag/$Cu_{20}Pd_{80}$ (Figure S2a, Supporting Information) and Ag/$Cu_{55}Pd_{45}$ (Figure S2b, Supporting Information), respectively. Furthermore, with the amount of Ag NPs and the molar ratio of $Pd(acac)_2$ to $Cu(acac)_2$ fixed, the shell thickness of CuPd could be tuned from 0.4 ± 0.05 nm (denoted as Ag/$Cu_{37}Pd_{63}$-0.4; Figure S3a, Supporting Information) to 1.1 ± 0.10 nm (denoted as Ag/$Cu_{37}Pd_{63}$-1.1; Figure S3b, Supporting Information) when 15 mg of $Pd(acac)_2$ and 13 mg of $Cu(acac)_2$ and when 60 mg of $Pd(acac)_2$ and 52 mg of $Cu(acac)_2$ were added, respectively. Similarly, when 3.1 nm Au (Figure S4a, Supporting Information) or 5 nm Au NPs (Figure S4b, Supporting Information) (see Experimental Methods and Computational Models) were used as seeding NPs, 4.6 ± 0.3 nm Au/CuPd (Figure 2c) or 7.0 ± 0.4 nm Au/CuPd NPs (Figure S4c, Supporting Information) with a 0.8 ± 0.05 nm shell were also prepared.

Figure S5 (Supporting Information) shows the XRD patterns of the face-centered cubic (*fcc*) Ag, Ag/$Cu_{20}Pd_{80}$, Ag/$Cu_{37}Pd_{63}$, and $Cu_{40}Pd_{60}$ NPs. The diffraction peaks from the Ag/CuPd core/shell NPs are between those from Ag and CuPd NPs, indicating that the formation of the core/shell structure leads to the expansion of CuPd lattice spacing.[44] High-resolution TEM (HRTEM) was used to analyze the detailed structure of a single Ag/CuPd NP, as shown in Figure 2d. The CuPd lattice fringes have a 0.224 nm spacing, close to {111} interplanar distance of *fcc*-CuPd (0.223 nm) but shorter than that of *fcc*-Ag (0.238 nm). The elemental distribution within the core/shell structure was characterized by aberration-corrected STEM-EELS (Figure 2e,f), showing that NPs contain Pd in the outside shell and Ag (or Au) in the core. It should be noted that, from the CuPd and CuAg phase diagram (Figure S6, Supporting Information), Cu forms an alloy much easier with Pd than with Ag. Therefore, Cu would stay in the shell of Ag/CuPd core/shell NPs but it cannot be detected easily by STEM-EELS in the thin CuPd shell.

Electrocatalysis of M/CuPd NPs. The electrocatalytic performance of the as-synthesized M/CuPd NPs were studied by cyclic voltammetry, the rotating disk electrode technique, and the current (i)–time (t) technique.[45] To perform these tests, the as-prepared NPs were first deposited on the Ketjen carbon support (EC-300J) via sonicating two constituents (the

dx.doi.org/10.1021/ja508256g | J. Am. Chem. Soc. 2014, 136, 15026–15033

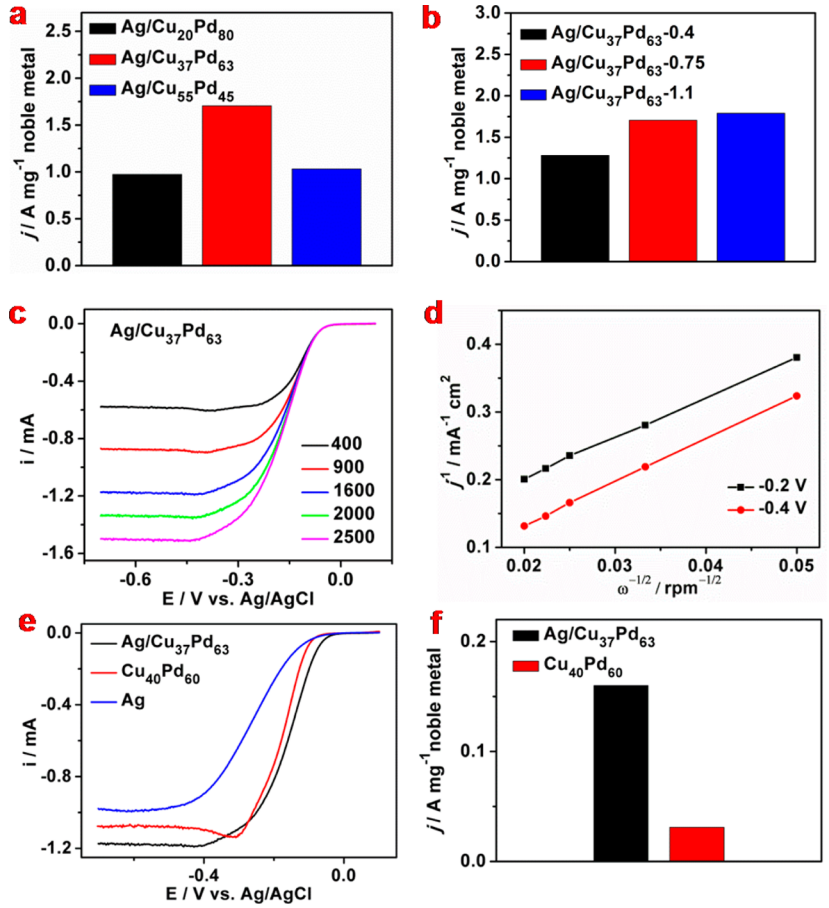

Figure 3. (a, b) Mass activity comparison at −0.2 V of Ag/CuPd NPs with different shell composition (a) and thickness (b) in O_2-saturated 0.1 M KOH solution at a scan rate of 10 mV/s. Rotation rate: 1600 rpm. (c) ORR polarization curves of $Ag/Cu_{37}Pd63$ NPs at different rotation rates; (d) K-L plots of the ORR from $Ag/Cu_{37}Pd_{63}$ NPs. (e, f) ORR polarization curves (e) and ORR mass activity summaries (f) at −0.1 V of $Ag/Cu_{37}Pd_{63}$, $Cu_{40}Pd_{60}$, and Ag NPs in O_2-saturated 0.1 M KOH solution at 293 K. Scan rate: 10 mV/s. Rotation rate: 1600 rpm.

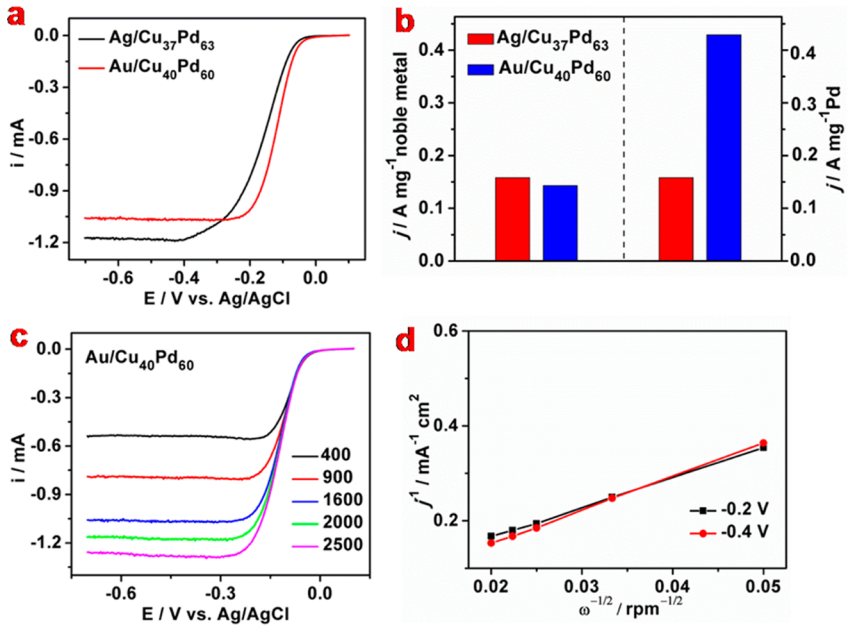

Figure 4. (a, b) ORR polarization curves (a) and ORR mass activity summaries (b) at −0.1 V of $Ag/Cu_{37}Pd_{63}$ and $Au/Cu_{40}Pd_{60}$ in O_2-saturated 0.1 M KOH solution at 293 K. Scan rate: 10 mV/s. Rotation rate: 1600 rpm. (c) ORR polarization curves of $Au/Cu_{40}Pd_{60}$ NPs at different rotation rates. (d) K-L plots of the ORR from $Au/Cu_{40}Pd_{60}$ NPs.

dx.doi.org/10.1021/ja508256g | J. Am. Chem. Soc. 2014, 136, 15026−15033

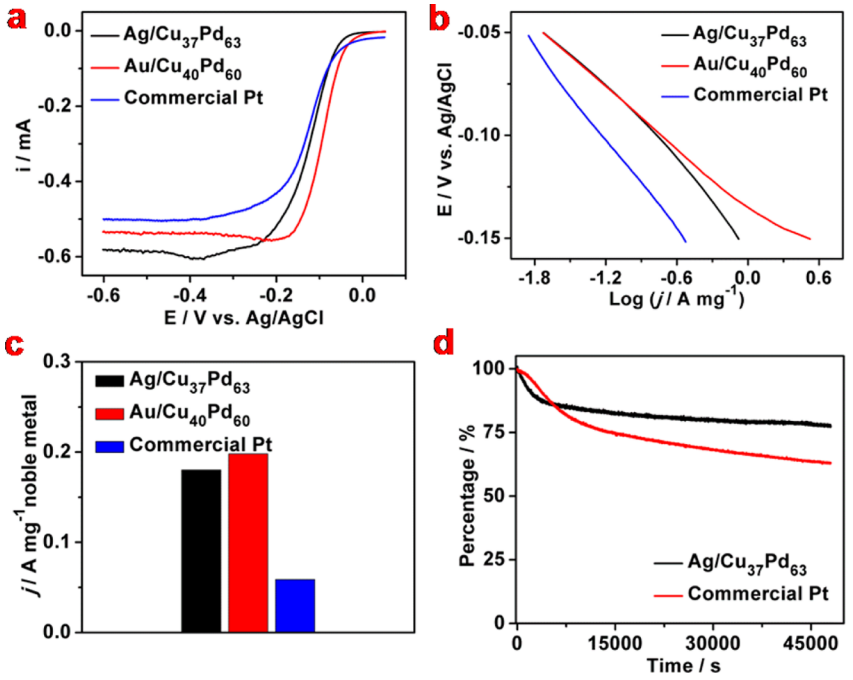

Figure 5. (a–c) ORR polarization curves (a), Tafel plots (b), and ORR mass activity summaries (c) at −0.1 V of $Ag/Cu_{37}Pd_{63}$, $Au/Cu_{40}Pd_{60}$, and commercial Pt in O_2-saturated 0.1 M KOH solution at 293 K. Scan rate: 10 mV/s. Rotation rate: 400 rpm. (d) Chronoamperometric responses for the ORR on $Ag/Cu_{37}Pd_{63}$ NPs and commercial Pt at −0.3 V. Rotation rate: 200 rpm.

mass ratio of NP to C is 1/2) in hexane[46,47] and then heated to 150 °C overnight to remove the surfactant according to the previous method.[28] These M/CuPd NPs were uniformly distributed on a carbon support, as shown in Figure S7 (Supporting Information) (denoted as C-M/CuPd). The treated C-NP catalysts were redispersed in deionized water/isopropyl alcohol/5% Nafion (4/1/0.05 v/v/v) to reach a concentration of 4 mg/mL. A 5 μL portion of the catalyst ink was casted on the surface of the GC electrode and dried under ambient conditions. Figure S8a (Supporting Information) and Figure 3a show typical ORR polarization curves (Figure S8a) and mass activity comparisons (Figure 3a) of the Ag/CuPd NPs with different shell compositions obtained at room temperature in O_2-saturated 0.1 M KOH. From Figure 3a, we can see that $Ag/Cu_{37}Pd_{63}$ NPs have the highest ORR activity among all Ag/CuPd NPs studied. The effect of the shell thickness of CuPd on the ORR activity of Ag/CuPd NPs was also investigated, as shown in Figure S8b (Supporting Information) and Figure 3b. The NPs with 0.75 nm shells have ORR activities similar to those with ∼1.1 nm shell but activities higher than those with 0.4 nm shells, which is consistent with our computational prediction.

Rotating disk electrode (RDE) measurements were used to study the ORR kinetics of the $Ag/Cu_{37}Pd_{63}$ NPs in 0.1 M KOH (Figure 3c). The number of electrons involved in the reduction of one O_2 molecule on the $Ag/Cu_{37}Pd_{63}$ NPs was determined via a combination of RDE techniques and the Koutecky–Levich (K-L) equation.[48] The corresponding K-L plots (Figure 3d) show the inverse current density (j^{-1}) as a function of the inverse of the square root of the rotation speed ($w^{-1/2}$) at different potential values. The number of electrons was determined to be about 4, indicating that the ORR on the Ag/CuPd NPs is a 4e process, similar to that on the commercial Pt catalyst measured in the same 0.1 M KOH solution.[48]

Figure 3e shows typical ORR polarization curves of $Ag/Cu_{37}Pd_{63}$, CuPd, and Ag NPs in O_2-saturated 0.1 M KOH. Both Ag NPs and $Cu_{40}Pd_{60}$ alloy NPs are less active than the $Ag/Cu_{37}Pd_{63}$ NPs for the ORR. After normalization of the activity against the amount of noble metals, the $Ag/Cu_{37}Pd_{63}$ NPs have a 5.2 times higher catalytic activity for ORR than the $Cu_{40}Pd_{60}$ NPs (Figure 3f). A comparison of the activity from $Ag/Cu_{37}Pd_{63}$, $Cu_{40}Pd_{60}$, and Ag NPs indicates that the core/shell NPs indeed show the synergistic core/shell effect on enhancing ORR catalytic activity.

According to the prediction that Au as the core material can further enhance CuPd ORR activity, we studied 4.6 nm $Au/Cu_{40}Pd_{60}$ NPs (0.8 nm CuPd shell) and compared their ORR activity with that of $Ag/Cu_{37}Pd_{63}$ NPs (0.75 nm CuPd shell) (Figure 4). The ORR performance of the CuPd shell is indeed enhanced by changing the core from Ag to Au (Figure 4a). When they were normalized against all noble metals in the core/shell structure, the mass activities of the $Au/Cu_{40}Pd_{60}$ NPs and $Ag/Cu_{37}Pd_{63}$ NPs obtained at a rotation of 1600 rpm have similar values (Figure 4b), but when only Pd is weighed in, the Au/CuPd NPs show a much higher mass activity (0.43 A/mg of Pd) than the Ag/CuPd NPs (0.16 A/mg of Pd) (Figure 4b). The ORR kinetics on the $Au/Cu_{40}Pd_{60}$ NPs was also analyzed, as shown in Figure 4c. The corresponding K-L plots (Figure 4**d**) give n = 4.0 from −0.2 to −0.4 V, revealing that the $Au/Cu_{40}Pd_{60}$ NPs still favor a 4e oxygen reduction process.

The ORR catalytic activity of the optimized Ag(Au)/CuPd NPs was further compared with that of the commercial Pt catalyst in the O_2-saturated 0.1 M KOH solution (Figure 5a). Both $Au/Cu_{40}Pd_{60}$ and $Ag/Cu_{37}Pd_{63}$ NPs have half-wave potentials more positive than that of the commercial Pt catalyst. In order to give quantitative information on the ORR activity of different catalysts, the corresponding Tafel plots (Figure 5b) and ORR mass activities at −0.1 V (normalized against all noble metals present in the catalyst) were

dx.doi.org/10.1021/ja508256g | J. Am. Chem. Soc. 2014, 136, 15026–15033

summarized (Figure 5c). Figure 5b gives a general information on how high a current density we can obtain at different potentials, while Figure 5c shows that the mass activities of the $Ag/Cu_{37}Pd_{63}$ (0.18 A/mg of Pd) and $Au/Cu_{40}Pd_{60}$ (0.20 A/mg of Au+Pd) obtained at the rotation of 400 rpm are nearly the same. As a comparison, the mass activity of the commercial Pt catalyst is only 0.06 A/mg of Pt under the same detection conditions (Figure 5c). The durability of the Ag/CuPd NPs and Pt was evaluated by using a chronoamperometric method at −0.30 V, a potential located at the mixed kinetic region (Figure 5d). The Ag/CuPd catalyst retains the higher current values (77.6% retention) than the Pt catalyst (62.9% retention) after a 48000 s $i-t$ test, demonstrating the longer-term stability of Au/CuPd over Pt. To the best of our knowledge, these $Ag/Cu_{37}Pd_{63}$ and $Au/Cu_{40}Pd_{60}$ catalysts are the best non-Pt catalysts developed for catalyzing the ORR in alkaline solution.

CONCLUSIONS

To summarize, our DFT calculations predict that M/CuPd (M = Ag, Au) NPs with 0.8 and 1.2 nm $CuPd_2$ shells have the optimal surface strain and composition to catalyze ORR. We prepared monodisperse M/CuPd NPs experimentally by coreduction of $Pd(acac)_2$ and $Cu(acac)_2$ in the presence of 3.1 nm Ag or Au seeds with shell thicknesses controlled at 0.4, 0.75, and 1.1 nm and compositions at $Cu_{20}Pd_{80}$, $Cu_{37}Pd_{63}$, and $Cu_{55}Pd_{45}$. These controls allow us to tune both shell electronic structure and surface strain to maximize ORR performance. In 0.1 M KOH solution, the $Au/Cu_{40}Pd_{60}$ and $Ag/Cu_{37}Pd_{63}$ catalysts with 0.75 and 1.1 nm shell coatings are more efficient for ORR than any other M/CuPd catalysts with different Cu/Pd compositions, CuPd NPs, and Ag studied in this paper. They have a mass activity of about 0.20 A/mg of noble metal that is over 3 times higher than that from the commercial Pt (0.06 A/mg of Pt). They also exhibit higher durability than the Pt catalyst, retaining 77.6% of their activity after 48000 s $i-t$ test (62.9% for the Pt catalyst). Our study highlights the important aspect of tuning surface strain and composition in the core/shell structure to maximize its ORR performance and to develop more advanced NP catalysts with ORR catalysis superior to that of Pt. The strategy demonstrated here can be extended to other core/shell systems, making it possible to design and tune NP catalysis for other important chemical reactions.

ASSOCIATED CONTENT

Supporting Information

Figure S1−S9, giving additional structures, TEM images, and plots. This material is available free of charge via the Internet at http://pubs.acs.org.

AUTHOR INFORMATION

Corresponding Authors

*E-mail for G.L.: ganglu@csun.edu.
*E-mail for S.S.: ssun@brown.edu.

Present Address

[‖]Physical Chemistry and Applied Spectroscopy, Los Alamos National Laboratory, Los Alamos, NM 87545, USA.

Notes

The authors declare no competing financial interest.

ACKNOWLEDGMENTS

This work was supported by the U.S. Army Research Laboratory and the U.S. Army Research Office under the Multi University Research Initiative (MURI, grant number W911NF-11-1-0353) on "Stress-Controlled Catalysis via Engineered Nanostructures". Electron microscopy work carried out at the Center for Functional Nanomaterials, Brookhaven National Laboratory, was supported by the U.S. Department of Energy, Office of Basic Energy Sciences, under Contract No. DE-AC02-98CH10886.

REFERENCES

(1) Voiry, D.; Yamaguchi, H.; Li, J.; Silva, R.; Alves, D. C. B.; Fujita, T.; Chen, M.; Asefa, T.; Shenoy, V. B.; Eda, G.; Chhowalla, M. *Nat. Mater.* **2013**, *12*, 850−855.
(2) Liu, M.; Zhang, R.; Chen, W. *Chem. Rev.* **2014**, *114*, 5117−5160.
(3) Ji, X.; Lee, K. T.; Holden, R.; Zhang, L.; Zhang, J.; Botton, G. A.; Couillard, M.; Nazar, L. F. *Nat. Chem.* **2010**, *2*, 286−293.
(4) Liang, Y.; Li, Y.; Wang, H.; Zhou, J.; Wang, J.; Regier, T.; Dai, H. *Nat. Mater.* **2011**, *10*, 780−786.
(5) Bing, Y.; Liu, H.; Zhang, L.; Ghosh, D.; Zhang, J. *Chem. Soc. Rev.* **2010**, *39*, 2184−2202.
(6) Chen, J.; Lim, B.; Lee, E. P.; Xia, Y. *Nano Today* **2009**, *4*, 81−95.
(7) Zhang, H.; Jin, M.; Xia, Y. *Chem. Soc. Rev.* **2012**, *41*, 8035−8049.
(8) Guo, S.; Zhang, S.; Sun, S. *Angew. Chem., Int. Ed.* **2013**, *52*, 8526.
(9) Stamenkovic, V. R.; Mun, B. S.; Arenz, M.; Mayrhofer, K. J. J.; Lucas, C. A.; Wang, G.; Ross, P. N.; Markovic, N. M. *Nat. Mater.* **2007**, *6*, 241−247.
(10) Stamenkovic, V. R.; Fowler, B.; Mun, B. S.; Wang, G.; Ross, P. N.; Lucas, C. A.; Marković, N. M. *Science* **2007**, *315*, 493−497.
(11) Norskov, J. K.; Bligaard, T.; Rossmeisl, J.; Christensen, C. H. *Nat. Chem.* **2009**, *1*, 37−46.
(12) Greeley, J.; Norskov, J. K.; Mavrikakis, M. *Rev. Phys. Chem.* **2002**, *53*, 319−348.
(13) Zhang, L.; Iyyamperumal, R.; Yancey, D. F.; Crooks, R. M.; Henkelman, G. *ACS Nano* **2013**, *7*, 9168−9172.
(14) Zhang, S.; Zhang, X.; Jiang, G.; Zhu, H.; Guo, S.; Su, D.; Lu, G.; Sun, S. *J. Am. Chem. Soc.* **2014**, *136*, 7734−7739.
(15) Strasser, P.; Koh, S.; Anniyev, T.; Greeley, J.; More, K.; Yu, C.; Liu, Z.; Kaya, S.; Nordlund, D.; Ogasawara, H.; Toney, M. F.; Nilsson, A. *Nat. Chem.* **2010**, *2*, 454−460.
(16) Mavrikakis, M.; Hammer, M. B.; Nørskov, J. K. *Phys. Rev. Lett.* **1999**, *81*, 2819.
(17) Norskov, J. K.; Rossmeisl, J.; Logadottir, A.; Lindqvist, L. *J. Phys. Chem. B* **2004**, *108*, 17886−17892.
(18) Stamenkovic, V.; Mun, B. S.; Mayrhofer, K. J. J.; Ross, P. N.; Markovic, N. M.; Rossmeisl, J.; Greeley, J.; Nørskov, J. K. *Angew. Chem., Int. Ed.* **2006**, *45*, 2897−2901.
(19) Lim, B.; Jiang, M.; Camargo, P. H. C.; Cho, E. C.; Tao, J.; Lu, X.; Zhu, Y.; Xia, Y. *Science* **2009**, *324*, 1302−1305.
(20) van der Vliet, D. F.; Wang, C.; Tripkovic, D.; Strmcnik, D.; Zhang, X. F.; Debe, M. K.; Atanasoski, R. T.; Markovic, N. M.; Stamenkovic, V. R. *Nat. Mater.* **2012**, *11*, 1051−1058.
(21) Cui, C.; Gan, L.; Heggen, M.; Rudi, S.; Strasser, P. *Nat. Mater.* **2013**, *12*, 765−771.
(22) Wang, C.; Chi, M.; Li, D.; Strmcnik, D.; van der Vliet, D.; Wang, G.; Komanicky, V.; Chang, K.-C.; Paulikas, A. P.; Tripkovic, D.; Pearson, J.; More, K. L.; Markovic, N. M.; Stamenkovic, V. R. *J. Am. Chem. Soc.* **2011**, *133*, 14396−14403.
(23) Kim, J.; Lee, Y.; Sun, S. *J. Am. Chem. Soc.* **2010**, *132*, 4996−4997.
(24) Wang, D.; Xin, H. L.; Hovden, R.; Wang, H.; Yu, Y.; Muller, D. A.; DiSalvo, F. J.; Abruña, H. D. *Nat. Mater.* **2013**, *12*, 81−87.
(25) Choi, S.-I.; Xie, S.; Shao, M.; Odell, J. H.; Lu, N.; Peng, H.-C.; Protsailo, L.; Guerrero, S.; Park, J.; Xia, X.; Wang, J.; Kim, M. J.; Xia, Y. *Nano Lett.* **2013**, *13*, 3420−3425.

(26) Snyder, J.; Fujita, T.; Chen, M. W.; Erlebacher, J. *Nat. Mater.* **2010**, *9*, 904−907.
(27) Sasaki, K.; Naohara, H.; Choi, Y.; Cai, Y.; Chen, W.-F.; Liu, P.; Adzic, R. R. *Nat. Commun.* **2012**, *3*, 1115.
(28) Wang, C.; van der Vliet, D.; More, K. L.; Zaluzec, N. J.; Peng, S.; Sun, S.; Daimon, H.; Wang, G.; Greeley, J.; Pearson, J.; Paulikas, A. P.; Karapetrov, G.; Strmcnik, D.; Markovic, N. M.; Stamenkovic, V. R. *Nano Lett.* **2011**, *11*, 919−926.
(29) Mazumder, V.; Sun, S. *J. Am. Chem. Soc.* **2009**, *131*, 4588−4589.
(30) Guo, S.; Li, D.; Zhu, H.; Zhang, S.; Markovic, N. M.; Stamenkovic, V. R.; Sun, S. *Angew. Chem., Int. Ed.* **2013**, *52*, 3465−3468.
(31) Zhu, H.; Zhang, S.; Guo, S.; Su, D.; Sun, S. *J. Am. Chem. Soc.* **2013**, *135*, 7130−7133.
(32) Koenigsmann, C.; Santulli, A. C.; Gong, K.; Vukmirovic, M. B.; Zhou, W.-P.; Sutter, E.; Wong, S. S.; Adzic, R. R. *J. Am. Chem. Soc.* **2011**, *133*, 9783−9795.
(33) Wu, G.; More, K. L.; Johnston, C. M.; Zelenay, P. *Science* **2011**, *332*, 443−447.
(34) Gong, K.; Du, F.; Xia, Z.; Durstock, M.; Dai, L. *Science* **2009**, *323*, 760−764.
(35) Tang, W.; Henkelman, G. *J. Chem. Phys.* **2009**, *130*, 194504−194509.
(36) Peng, S.; Lee, Y.; Wang, C.; Yin, H.; Dai, S.; Sun, S. *Nano Res.* **2008**, *1*, 229−234.
(37) Ho, S. F.; Mendoza-Garcia, A.; Guo, S.; He, K.; Su, D.; Liu, S.; Metin, Ö.; Sun, S. *Nanoscale* **2014**, *6*, 6970−6973.
(38) Zhou, X. W.; Johnson, R. A.; Wadley, H. N. G. *Phys. Rev. B* **2004**, *69*, 144113−144122.
(39) Kresse, G.; Hafner, J. *Phys. Rev. B* **1993**, *47*, 558−561.
(40) Kresse, G.; Furthmuller, J. *Phys. Rev. B* **1996**, *54*, 11169−11186.
(41) Blochl, P. E. *Phys. Rev. B* **1994**, *50*, 17953−17979.
(42) Perdew, J. P.; Burke, K.; Ernzerhof, M. *Phys. Rev. Lett.* **1996**, *77*, 3865−3868.
(43) Monkhorst, H. J.; Pack, J. D. *Phys. Rev. B* **1976**, *13*, 5188−5192.
(44) Mazumder, V.; Chi, M.; More, K. L.; Sun, S. *Angew. Chem., Int. Ed.* **2010**, *49*, 9368−9372.
(45) Guo, S.; Zhang, S.; Wu, L.; Sun, S. *Angew. Chem., Int. Ed.* **2012**, *51*, 11770−11773.
(46) Guo, S.; Zhang, S.; Sun, X.; Sun, S. *J. Am. Chem. Soc.* **2011**, *133*, 15354−15357.
(47) Zhang, S.; Guo, S.; Zhu, H.; Su, D.; Sun, S. *J. Am. Chem. Soc.* **2012**, *134*, 5060−5063.
(48) Wang, S.; Zhang, L.; Xia, Z.; Roy, A.; Chang, D. W.; Baek, J.-B.; Dai, L. *Angew. Chem., Int. Ed.* **2012**, *51*, 4209−4212.